Journal of Materials Chemistry A

PAPER

View Article Online
View Journal | View Issue

Fabrication of one-dimensional heterostructured TiO_2@SnO_2 with enhanced photocatalytic activity†

Cite this: *J. Mater. Chem. A*, 2014, **2**, 116

Xin Xu,‡[a] Guorui Yang,‡[b] Jin Liang,[a] Shujiang Ding,*[a] Chengli Tang,[b] Honghui Yang,[b] Wei Yan,[bc] Guidong Yang*[d] and Demei Yu*[a]

Received 24th July 2013
Accepted 14th October 2013

DOI: 10.1039/c3ta12863f

www.rsc.org/MaterialsA

TiO_2@SnO_2 nanosheets@nanotubes heterostructures were successfully prepared by a facile two-step method: prefabricated SnO_2@PNT coaxial nanocables based on the *in situ* growth of SnO_2 in the sulfonated gel matrix of polymeric nanotubes, and then the assembly of TiO_2 nanoclusters that consist of ultrathin nanosheets through a solvothermal process. These heterostructures were characterized for the morphological, structural and optical properties by scanning electron microscopy (SEM), transmission electron microscopy (TEM), X-ray diffraction (XRD), X-ray photoelectron spectroscopy (XPS), UV-visible (UV-vis) and diffuse reflectance spectroscopy (DRS). The photocatalytic investigations showed that the TiO_2@SnO_2 heterostructures possessed enhanced photocatalytic efficiency in the photodegradation of Rhodamine B (RhB) and photocatalytic H_2 evolution from water splitting under ultraviolet (UV) light irradiation, compared with the pristine TiO_2 nanosheets, SnO_2 nanotubes, the mechanically mixed two samples and P25. The enhanced photocatalytic performance can be ascribed to the beneficial microstructure and synergistic effects of coupled TiO_2@SnO_2 nanosheets@nanotubes heterostructures.

1. Introduction

Photocatalysis has attracted a great deal of attention as a promising candidate for the elimination of organic contaminants in water and air, since the pioneering work by Honda and Fujishima.[1] Titanium dioxide (TiO_2) has and continues to be one of the most widely studied semiconductors for photocatalytic applications due to its advantages, such as a suitable band gap for redox reactions, long-term stability, low cost, non-toxicity and so on.[2,3] However, as a single component semiconductor photocatalyst, TiO_2 has an inherent drawback that the photogenerated electron/hole (e^-/h^+) pairs recombine fast (~10 ns)[4] and hence only a fraction of e^-/h^+ pairs are available for the photoreaction. To date, this disadvantage can be overcome by means of semiconductor coupling.[5] With this approach, the assembled semiconductors are selected suitably so that efficient charge transfer occurs between them. This condition spatially separates the photoexcited electrons and holes onto the different constituents and reduces the rate of e^-/h^+ pair recombination.[6]

In recent years, various coupled semiconductor systems based on TiO_2 have been developed, such as SnO_2/TiO_2,[7–10] ZnO/TiO_2,[11] WO_3/TiO_2,[12] CdS/TiO_2,[13] Fe_2O_3/ZnO[14] and so on. In particular, the SnO_2/TiO_2 system with high photocatalytic activity has attracted extensive interest. SnO_2 possesses a high electron mobility (~100–200 $cm^2\ V^{-1}\ s^{-1}$),[15] indicating a faster transport of photoexcited electrons.[16] Moreover, the conduction-band edge of SnO_2 is more positive than that of TiO_2, leading to the migration of photoexcited electrons from the conduction band of TiO_2 to that of SnO_2,[17–20] consequently the recombination of charge carriers can be suppressed, thereby resulting in a higher photocatalytic performance.[21–23] Aerosol assisted chemical vapour deposition was also introduced to synthesize a TiO_2–SnO_2 composite film, and the as-prepared TiO_2–SnO_2 film exhibited enhanced photocatalytic activity over the degradation of dye compared to the TiO_2 film and SnO_2 film.[22] Gao *et al.* demonstrated that the power conversion efficiency value of the SnO_2–TiO_2 core–shell structured DSSCs is above five times higher than that of SnO_2 nanotubes.[24] Zhang *et al.* reported a novel-structured TiO_2/SnO_2 hybrid nanofiber photocatalyst with enhanced photocatalytic activity prepared *via* the electrospinning method, the heterostructures promote the photogenerated e^-/h^+ pairs separation.[25]

[a]*State Key Laboratory for Mechanical Behavior of Materials, MOE Key Laboratory for Nonequilibrium Synthesis and Modulation of Condensed Matter and Department of Applied Chemistry, School of Science, Xi'an Jiaotong University, Xi'an 710049, China. E-mail: dingsj@mail.xjtu.edu.cn; dmyu@mail.xjtu.edu.cn*

[b]*Department of Environmental Science & Engineering, Xi'an Jiaotong University, Xi'an 710049, China*

[c]*State Key Laboratory of Multiphase Flow in Power Engineering, Xi'an Jiaotong University, Xi'an 710049, China*

[d]*Department of Chemical Engineering, School of Chemical Engineering and Technology, Xi'an Jiaotong University, Xi'an, 710049, China. E-mail: guidongyang@mail.xjtu.edu.cn*

† Electronic supplementary information (ESI) available. See DOI: 10.1039/c3ta12863f

‡ Xin Xu and Guorui Yang contributed equally to this work.

To date, numerous types of coupled SnO_2/TiO_2 systems, such as particle,[26] composite film,[27] stacks,[15] core–shell heterostructures[28] and so on, have been successfully obtained. However the particle-like morphology photocatalyst is very inconvenient for recycling due to its extreme dispersive property and it may cause secondary pollution. On the other hand, the film-type photocatalyst increases the recovery efficiency at the expense of the specific surface area, resulting in a low photocatalytic activity. One-dimensional (1D) structures, such as nanowires, nanobelts and nanotubes, have attracted tremendous attention within the last decade. One promising approach to overcoming these drawbacks simultaneously is to use 1D photocatalysts, which provide a relatively large specific surface area as compared with nanoparticles, and are recycled easily due to the large length to diameter ratio. Among the huge variety of 1D nanostructures, semiconducting nanotubes are particularly interesting, not only for fundamental research due to the unique hollow structural and physical properties relative to their bulk counterparts, but also for their fascinating potential in optoelectronic and electronic devices. More importantly, it has been proven that the 1D nanomaterials effectively support the direct growth of secondary nanostructures by heterogeneous nucleation because of their porous surface and large surface area.[29–31]

In this work, we employ polymeric nanotubes (PNTs) with uniform size, synthesized by the cationic polymerization of divinylbenzene using immiscible initiator nanodroplets of boron trifluoride etherate complex as hard templates after sulfonation.[32] The synthetic process is illustrated in Scheme 1. Firstly, we prefabricated SnO_2@PNT coaxial nanocables based on the *in situ* growth of SnO_2 in the sulfonated gel matrix of polymeric nanotubes.[33–37] Then the SnO_2@PNT coaxial nanocables were assembled by TiO_2 nanoclusters that consist of ultrathin nanosheets after a solvothermal process. After being calcined in air, the hierarchically structured TiO_2@SnO_2 composite was successfully obtained. Moreover, the uniform PNTs used in this work have three main advantages as templates: (i) the positively charged precursor ions can be easily adsorbed to the surface of the sulfonated PNTs due to the electrostatic interaction with the negative functional groups ($-SO_3$); (ii) PNTs can be easily removed through calcination at a lower temperature, by which the nanostructure of the metal oxide can be well preserved; (iii) the produced gas and osmotic pressure during the calcination can be released through the inner channels and open ends of the PNTs.[33]

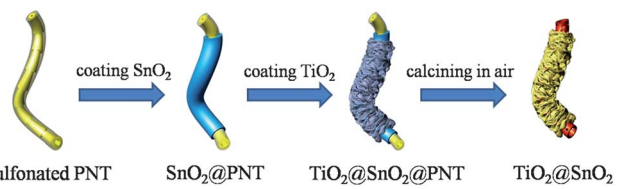

Scheme 1 Schematic illustration of the synthetic procedure of the TiO_2@SnO_2 composite.

2. Experimental

2.1 Material synthesis

2.1.1 Sulfonated PNTs. Polymeric nanotubes (PNTs) were prepared according to a previously reported method.[32] PNTs (3 g) were added to concentrated sulfuric acid (polymeric nanotubes: H_2SO_4 = 1 : 30, w/w) and the mixture was ultrasonicated for 10 min to disperse them. After stirring for 24 h at 40 °C the yellow precipitate was collected by centrifugation and washed thoroughly with ethanol.

2.1.2 SnO_2@PNT. Acid-treated polymeric nanotubes (100 mg) were dispersed into a 20 mM mercaptoacetic acid solution (40 mL) by sonication for 10 minutes, followed by the addition of $SnCl_2$ (100 mg), urea (0.5 g), and HCl solution (37 wt %, 0.5 mL). The reaction mixture was then transferred into a 100 mL round bottom flask. After stirring for 6 h at 60 °C, the flask was left to cool to room temperature. The precipitate was collected by centrifugation, washed thoroughly with ethanol, and dried at 60 °C overnight.

2.1.3 TiO_2@SnO_2@PNT. 200 mg of the SnO_2@PNT synthesized using the previous method was dispersed in 40 mL of isopropyl alcohol (IPA) by sonication for 10 min, followed by the addition of 0.03 mL of DETA. After gentle stirring for 2 min, 1.5 mL of TIP was added. The solution was then transferred into a 60 mL Teflon-lined stainless steel autoclave and kept in an electric oven at 200 °C for 24 h. The autoclave was then taken out of the oven and left to cool down to room temperature. The precipitate was collected by centrifugation, washed thoroughly with ethanol, and dried at 60 °C overnight.

2.1.4 TiO_2@SnO_2. To obtain the TiO_2@SnO_2, the as-prepared composite was subjected to calcination at 450 °C for 2 h to remove the PNT template and obtain the hierarchically structured TiO_2@SnO_2 composite.

2.2 Characterization

The product morphology was examined using field-emission scanning electron microscopy (FESEM; HITACHI, su-8010) and transmission electron microscopy (TEM; JEOL, JEM-2100). Crystallographic information of the samples was collected using powder X-ray diffraction (XRD; SHIMADZU, Lab X XRD-6000). The chemical states of the products were studied using the X-ray photoelectron spectroscopy (XPS) measurement performed on an Axis Ultra, Kratos (UK) at monochromatic Al Kα radiation (150 W, 15 kV and 1486.6 eV). The vacuum in the spectrometer was 10–9 Torr. Binding energies were calibrated relative to the C 1s peak (284.6 eV). Thermogravimetric analysis (Perkin-Elmer TGA 7) was carried out under a flow of air with a temperature ramp of 20 °C min^{-1} from room temperature to 600 °C. The specific surface area and pore size distribution of the products were measured using a BET analyzer (ASAP 2020M) at 77 K.

2.3 Photocatalytic tests

The photocatalytic performance of the as-fabricated products was studied by degrading Rhodamine B (RhB) in simulated wastewater under UV irradiation. The photocatalytic

experiments were conducted in a homemade quartz photochemical reactor with a quartz jacket and cooled off by circulating water. In the experiment, a 500 W xenon lamp with a cutoff filter (λ < 420 nm) was employed as the ultraviolet light source; the distance between the xenon lamp and the front surface of the reactor was fixed to be 8 cm. For comparison, the mechanically mixed SnO_2 nanotubes with TiO_2 nanosheets (the weight ratio of SnO_2: TiO_2 = 1:4, which is similar to that of TiO_2@SnO_2 composite), and which is labeled as SnO_2 + TiO_2, was studied as a reference.

2.3.1 Photocatalytic RhB degradation. Prior to illumination, 50 mL of RhB aqueous solutions (10 mg L^{-1}) containing 0.05 g samples were magnetically stirred in the dark for 30 min to achieve adsorption/desorption equilibrium and good dispersion. During irradiation, about 3.0 mL of the reaction solution was withdrawn from the reactor at intervals of 10 mins and centrifuged to separate the photocatalyst. The supernatant solution was analyzed by an Agilent 8430 UV-vis spectrophotometer at λ = 554 nm, which is the maximum absorption wavelength of RhB. The remaining RhB concentration (%) after various intervals of time could be estimated using the following equation:

$$\%\text{RhB concentration} = C/C_0 \times 100\%$$

where C_0 is the initial concentration of RhB aqueous solution (that is, after the dark adsorption equilibrium), while C is the concentration at the illumination time t min. The control experiment indicates that RhB can be slightly degraded under UV light irradiation without a catalyst, suggesting that the photocatalytic process was primarily responsible for the RhB degradation.

2.3.2 Photocatalytic H_2 evolution from water splitting. In each experiment, 0.05 g of photocatalyst was dispersed in a 50 mL aqueous solution containing 0.25 M Na_2S and 0.35 M Na_2SO_3 which acted as sacrificial agents to protect photocatalysts from the photocorrosion process. The light intensity reaching the surface of the reaction solution was tested to be 145 mW cm^{-2}. Before irradiation, the system was bubbled with nitrogen for 30 min to remove the air inside and to ensure that the reaction system is under anaerobic conditions. The amount of H_2 evolution was determined on a gas chromatograph (Agilent Technologies: 6890N) with TCD (Thermal Conductivity Detector) equipped with a 5 Å molecular sieve using N_2 as the carrier gas. Blank experiments revealed that no hydrogen was produced without the addition of the catalysts or light irradiation.

3. Results and discussion

Fig. 1 shows the morphology of the acid-treated PNTs and SnO_2@PNT composite. It can be seen from the scanning electron microscope (SEM) image of the acid-treated PNTs that these templates are about 100–250 nm in diameter (Fig. 1A). The transmission electron microscopy (TEM) image indicates that the acid-treated PNTs possess an extremely smooth surface (Fig. 1B). The morphology of the SnO_2@PNT is shown in Fig. 1C and D. It can be observed that the diameter of the acid-treated

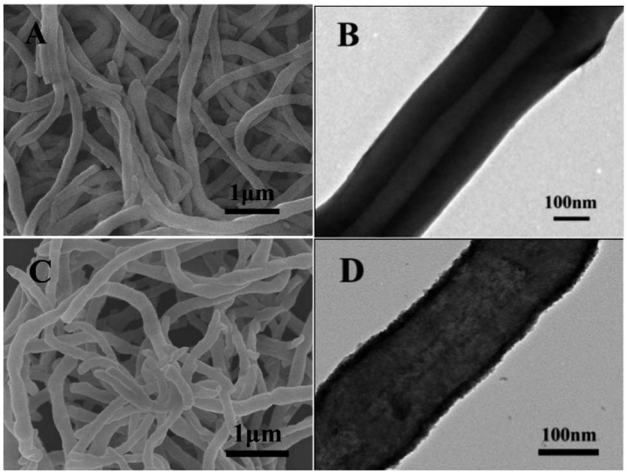

Fig. 1 (A) SEM image and (B) TEM image of the sulfonated PNTs; (C) SEM image and (D) TEM image of the SnO_2@PNT composite.

PNTs increases to approximately 125–275 nm (Fig. 1C), the surface of the SnO_2@PNT composite becomes much rougher than the PNTs before coating with SnO_2, and the thickness of the SnO_2 layer is approximately 15–25 nm (Fig. 1D).

Fig. 2 shows the SEM and TEM images of the TiO_2@SnO_2@PNT and TiO_2@SnO_2 composites. The TiO_2@SnO_2@PNT composite displays a tubular structure with a diameter of around 500–600 nm (Fig. 2A). The TEM image shows that the SnO_2@PNT nanotubes are uniformly assembled by TiO_2 nanoclusters that consist of ultrathin nanosheets (Fig. 2B), and the heights of

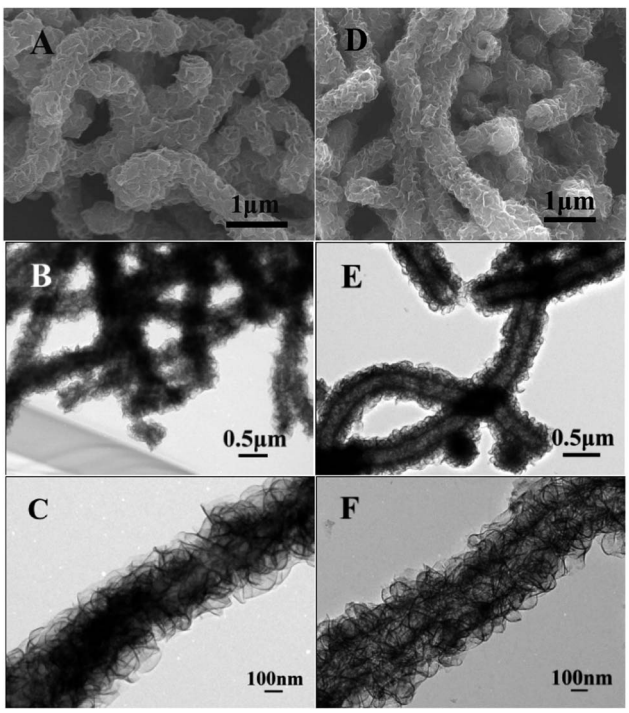

Fig. 2 (A) SEM image; (B and C) TEM images of TiO_2@SnO_2@PNT composite; (D) SEM image; (E and F) TEM images of TiO_2@SnO_2 composite after calcining the TiO_2@SnO_2@PNT composite at 450 °C for 2 h.

these TiO_2 nanosheets are about 225–475 nm through calculation. A hierarchical structure of the TiO_2@SnO_2@PNT composite's surface can be clearly revealed from the TEM image (Fig. 2C). The formation of the TiO_2 nanosheets could be explained by the dual function of diethylenetriamine (DETA): catalyzing the hydrolysis of titanium (IV) is opropoxide (TIP) to form TiO_2 nanosheets and assisting the self-assembly of the formed TiO_2 nanostructures on the surface of SnO_2@PNT, possibly through electrostatic interactions.[38,39] Fig. 2D shows the SEM image of the TiO_2@SnO_2 composite obtained after calcining the TiO_2@SnO_2@PNT composite at 450 °C for 2 h. The diameter of the hierarchically structured TiO_2@SnO_2 composite is approximately 450–550 nm, smaller than the TiO_2@SnO_2@PNT composite, possibly because of the partial collapse of the hollowed TiO_2@SnO_2 structure during the annealing process. The calcined TiO_2@SnO_2 composite maintains its tubular and sheet-like structures after removing the PNT templates. The TEM image of the calcined TiO_2@SnO_2 composite displays that the sample has an extra porous structure of the inside nanotubes, and the thickness of the TiO_2 nanosheets is approximately 10 nm (Fig. 2E and F). It is noteworthy that the ultrasonic process before TEM observation was unable to cause TiO_2 nanosheets to fall off from the SnO_2 nanotubes, which may suggest that a compact interface was established between the TiO_2 and SnO_2. As shown in the HRTEM image of Fig. S1,† we can see the clear interface between the SnO_2 and TiO_2. Moreover, the XPS data further confirmed the composition of the heterostructured TiO_2@SnO_2 composite (Fig. S2†).

The chemical composition of the different samples was characterized by using X-ray diffraction (XRD; Fig. 3A). It is clear from the patterns of curve I and curve II that pure TiO_2 nanosheets and pristine SnO_2 nanotubes can be assigned to anatase TiO_2 (JCPDS card no. 21-1272) and rutile SnO_2 (JCPDS card no. 41-1445). All the diffraction peaks of curve I and curve II can be discovered from curve III clearly, indicating that SnO_2 and TiO_2 successfully formed on the surface of acid-treated PNTs. The weight fraction of SnO_2 and TiO_2 in the hybrid material was determined by thermogravimetric analysis (TGA), with the results shown in Fig. 3B. The SnO_2@PNT and TiO_2@SnO_2@PNT composites show significant weight loss at about 450 °C, which is attributed to the combustion of the acid-treated PNT templates. After reaching 600 °C, the SnO_2@PNT and TiO_2@SnO_2@PNT composites show a total weight loss of 79.3% and 44.0%, respectively. The mass ratio of SnO_2 and TiO_2 calculated from the two curves is about 1:4.

Fig. 4A shows the solid diffuse reflection UV-vis spectrum (DRS) of the SnO_2 nanotubes, TiO_2 nanosheets and TiO_2@SnO_2 composite. A strong absorption edge at *ca.* 395 nm appears in the absorption spectrum of the TiO_2@SnO_2 composite, while the onset of the absorption of the TiO_2 nanosheets and SnO_2 nanotubes were 385 nm and 375 nm. According to the formula of the band gap ($E_g = 1240/\lambda$),[13] the band-gap values of TiO_2@SnO_2 composite, TiO_2 nanosheets and SnO_2 nanotubes were calculated to be 3.15 eV, 3.21 eV and 3.42 eV. The absorption edge of the TiO_2@SnO_2 composite was red-shifted compared to the TiO_2 nanosheets and SnO_2 nanotubes, which

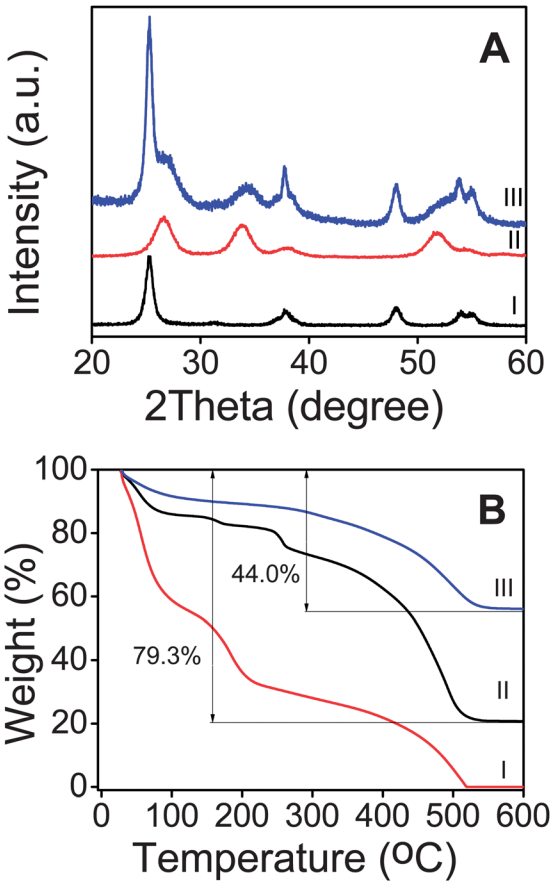

Fig. 3 (A) XRD patterns of the TiO_2 nanosheets (I), SnO_2 nanotubes (II) and TiO_2@SnO_2 composite and (B) TGA analysis of the pure sulfonated PNTs (I), SnO_2@PNT composite (II) and TiO_2@SnO_2@PNT composite (III).

reflects that the electronic structure and optical properties of the bare TiO_2 or SnO_2 have been modified. This is presumably because the TiO_2 was doped by a fraction of the Sn on the interface between the TiO_2 and SnO_2 during the final annealing process,[40] or the effective coupling of SnO_2 and TiO_2,[11] and results in the red-shifting of the absorption edge in the TiO_2@SnO_2 composite.

Fig. 4B shows the degradation profiles of the Rhodamine B (RhB) wastewater under ultraviolet light (UV) with various photocatalysts. As one can see, the degradation of RhB by the pure SnO_2 nanotubes is the least significant among all the catalysts, and only about 82.0% of RhB was degraded in 60 min. This is primarily ascribed to the wide band gap of SnO_2, leading to a limited absorption of photons. In comparison, the samples of TiO_2 nanosheets and mechanically mixed SnO_2 nanotubes with TiO_2 nanosheets exhibit higher activities, with a degradation rate of 88.9% and 90.3% for RhB, respectively. The improved activity can be assigned to the narrow band gap of the TiO_2. The degradation efficiency of P25 reaches 94.5%, which is higher than the TiO_2 nanosheets due to the coexistence and optimal ratio of rutile and anatase TiO_2. The TiO_2@SnO_2 composite exhibits the best performance of the photodegradation of RhB among the as-prepared samples, and

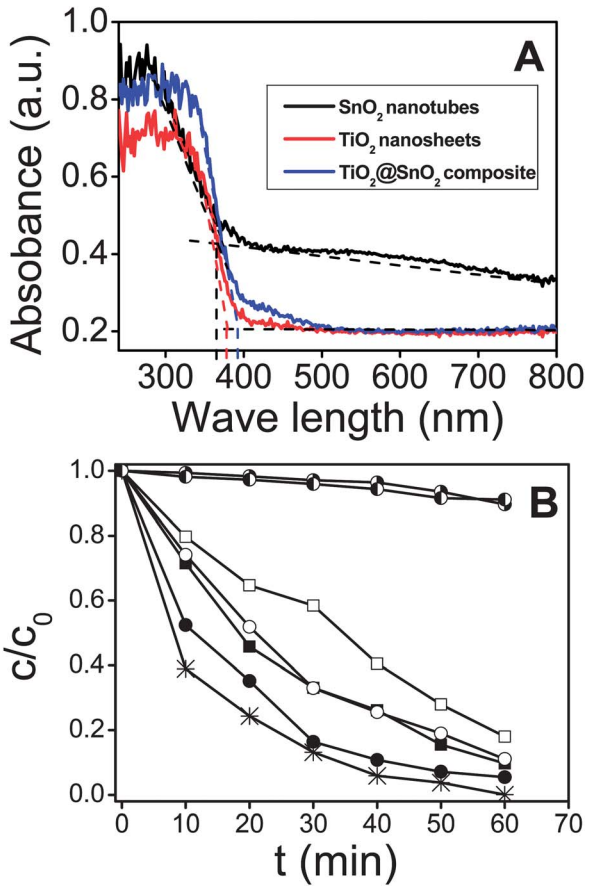

Fig. 4 (A) DRS of the SnO_2 nanotubes, TiO_2 nanosheets and TiO_2@SnO_2 composite, (B) degradation profiles of RhB over different samples: SnO_2 nanotubes (□), TiO_2 nanosheets (○), SnO_2 + TiO_2 mixture (■), P25 (●), TiO_2@SnO_2 composite (*), without photocatalyst (◑) and without UV light (◐).

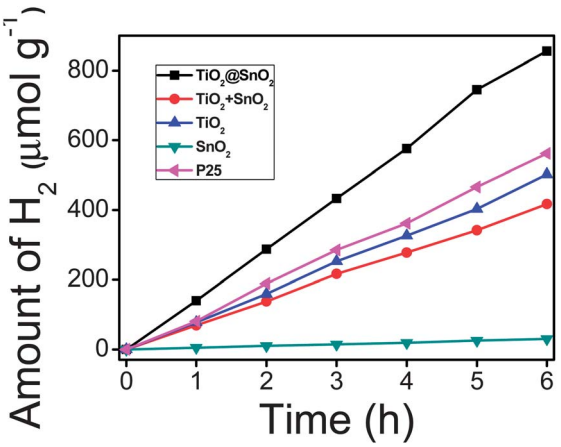

Fig. 5 Photocatalytic H_2 production efficiency of samples TiO_2@SnO_2, TiO_2 + SnO_2, TiO_2 nanosheets, SnO_2 nanotubes and P25.

almost 100% of the RhB molecules decomposed in 60 min. To investigate the degradation kinetics of RhB in solution and quantitatively compare the photocatalytic performances of these samples, the pseudo first-order equation was adopted to describe the experimental data because of the low initial concentrations of the substrates as follows: $\ln(C_0/C) = kt$, where k is a reaction rate constant. As can be seen in Fig. S3,† the order of the k values, which is derived from the plots of $\ln(C_0/C)$ *versus* irradiation time (t), is summarized as follows: TiO_2@SnO_2 composite > P25 > TiO_2 + SnO_2 mixture > TiO_2 nanosheets > SnO_2 nanotubes. This is in good agreement with the results presented in Fig. 4B. In addition to organic pollutants removal, photocatalytic H_2 generation was also observed over the SnO_2@TiO_2 heterostructures. As illustrated in Fig. 5, the H_2 evolution over the SnO_2@TiO_2 heterostructures was significantly higher than that of the bare SnO_2 nanotubes, pristine TiO_2 nanosheets, the mechanically mixed two samples and P25 throughout the 6 h of UV light irradiation, which is similar to the photocatalytic efficiency. These outcomes demonstrated that the SnO_2@TiO_2 heterostructures obtained in this work possess excellent properties in both photo-oxidation and photo–reduction reactions.

The reasons for the high photocatalytic performance of the sample TiO_2@SnO_2 could be explained in detail as follows: (i) SnO_2@TiO_2 heterostructures have a large specific surface area (124 m^2 g^{-1}) compared with SnO_2 nanotubes (102 m^2 g^{-1}).[33] As is known, nanomaterials with larger specific surface areas could offer more active sites and absorb more oxygen, which leads to a higher photocatalytic performance.[9] (ii) The band alignment between SnO_2 and TiO_2 is generally classified as a type II structure (staggered band alignment between these two different materials).[41] In this band-gap configuration, when photogenerated e^-/h^+ pairs are generated in SnO_2 nanotubes and TiO_2 nanosheets, the electrons on the TiO_2 particle surface transfer swiftly to the conduction band of SnO_2 *via* interfaces; similarly, the holes on the SnO_2 surface migrate to TiO_2 owing to the different valence band edge. The probability of the recombination of the photogenerated e^-/h^+ pairs is retarded at the same time. When the heterojunctions between SnO_2 and TiO_2 are formed, the Fermi energies in the boundary between the SnO_2 and TiO_2 phases should be matched.[42] This leads to the potential of the conduction band and valence band of SnO_2 to be more negative.[43,44] (see Fig. S2 E in the ESI†) Therefore, the conduction band position of SnO_2 will meet the requirements of the hydrogen evolution reaction.[45] Moreover, the nanosheets/nanotubes-type structure possesses a large interfacial region, which can improve the charge carrier separation to a large extent.[46] (iii) The nanosheets-nanotubes structures could improve the photon utilization efficiency. When the surfaces of the TiO_2@SnO_2 composite was irradiated with light, some of the incident photons were directly absorbed by SnO_2 and TiO_2, some were reflected and scattered, multiplied by the nanotubes and nanosheets. Hence, along with the increase in effective optical path length, the photon–matter interaction length multiplies, leading to a higher light harvesting based on the Beer–Lambert Law.[47–49] (iv) The unique 1D TiO_2@SnO_2 heterostructures obtained in this work could prevent the photo induced agglomeration and result in low boundary density,[50] thereby leading to the decrease of the recombination centre. This could be proven by the SEM images of the sample after

catalytic reaction (Fig. S4†). (v) The TiO_2@SnO_2 composite has an obvious red shift of *ca.* 10–20 nm in the absorption edge, compared with the pure SnO_2 nanotubes and TiO_2 nanosheets. This larger absorption edge would lead to the enhancement of the photocatalytic performance of the TiO_2@SnO_2 composite.[51]

From the viewpoint of practical application, it is crucial that the as-prepared photocatalyst maintains a high activity and stability for long-term use. As Fig. 6 illustrates, the TiO_2@SnO_2 composite photocatalyst possessed a sustainable photocatalytic performance in H_2 generation after 4 cycles. There was insignificant loss of the H_2 evolution rate, which indicates that the TiO_2@SnO_2 heterostructures were highly stable and reusable. The SEM images of the TiO_2@SnO_2 after the photocatalytic process display that the TiO_2@SnO_2 still retain the original morphology even after four recycles without any detected agglomeration or damage (Fig. S4†). Moreover, at the end of the reaction when the mixing was stopped, the TiO_2@SnO_2 composite photocatalyst can be easily separated from the solution by sedimentation, thus indicating it has good separation characteristics, which may be due to the large length to diameter ratio of the TiO_2@SnO_2 lD heterostructures.

4. Conclusions

In summary, a TiO_2@SnO_2 composite has been successfully prepared by a facile two-step method. SEM, TEM, XRD and XPS analysis revealed the successful coating of TiO_2 nanosheets on the surface of SnO_2 nanotubes. In comparison with the uncoated SnO_2 nanotubes, pure TiO_2 nanosheets, the mechanically mixed two samples and P25, the TiO_2@SnO_2 composite exhibited the best photocatalytic performance for the decomposition of RhB and photocatalytic H_2 production over water splitting under UV light irradiation. In particular, 1D TiO_2@SnO_2 composites processed several excellent properties including a relatively large specific surface area for supplying abundant active sites, suitable band engineering for charge carriers separation and unique 1D heterostructures for resistance to photo induced agglomeration. We assumed that the synergistic effects of the aforementioned factors contributed to the enhance photocatalytic performance of the 1D TiO_2@SnO_2 heterostructures.

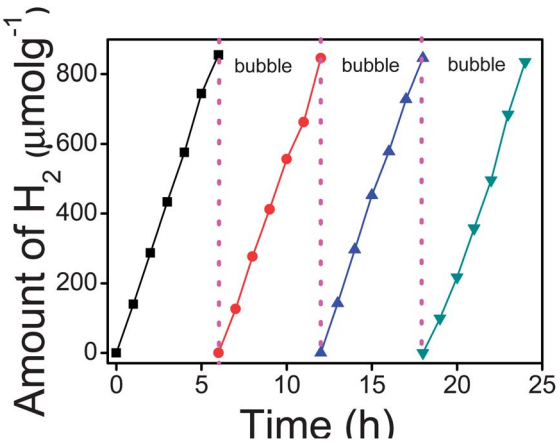

Fig. 6 Reuse cycles of photocatalytic H_2 generation over the sample TiO_2@SnO_2 composite; every 6 h the reaction system was bubbled with N_2 for 30 min to remove the H_2 inside.

Acknowledgements

This research was supported partially by the National Natural Science Foundation of China (no. 51273158, 21303131); Natural Science Basis Research Plan in Shaanxi Province of China (no. 2012JQ6003); Fundamental Research Funds for the Central Universities of China (2011JDGZ15, xjj2012092, 2012jdhz34) and Natural science fund of Jiangsu Province, China (SBK201022919).

References

1 A. Fujishima and K. Honda, *Nature*, 1972, **238**, 37–38.
2 H. B. Wu, H. H. Hng and X. W. Lou, *Adv. Mater.*, 2012, **24**, 2567–2571.
3 J. S. Chen, C. P. Chen, J. Liu, R. Xu, S. Z. Qiao and X. W. Lou, *Chem. Commun.*, 2011, **47**, 2631–2633.
4 R. Sasikala, A. Shirole, V. Sudarsan, T. Sakuntala, C. Sudakar, R. Naik and S. R. Bharadwaj, *Int. J. Hydrogen Energy*, 2009, **34**, 3621–3630.
5 L. Xu, E. M. P. Steinmiller and S. E. Skrabalak, *J. Phys. Chem. C*, 2012, **116**, 871–877.
6 W. L. Yang, L. Zhang, Y. Hu, Y. J. Zhong, H. B. Wu and X. W. Lou, *Angew. Chem., Int. Ed.*, 2012, **51**, 11501–11504.
7 H. A. J. L. Mourão, W. A. Junior and C. Ribeiro, *Mater. Chem. Phys.*, 2012, **135**, 524–532.
8 K. Vinodgopal, I. Bedja and P. V. Kamat, *Chem. Mater.*, 1996, **8**, 2180–2187.
9 H. Tada, A. Hattori, Y. Tokihisa, K. Imai, N. Tohge and S. Ito, *J. Phys. Chem. B*, 2000, **104**, 4585–4587.
10 Y. A. Cao, X. T. Zhang, W. S. Yang, H. Du, Y. B. Bai, T. J. Li and J. N. Yao, *Chem. Mater.*, 2000, **12**, 3445–3448.
11 P. F. Du, L. X. Song, J. Xiong, N. Li, Z. Q. Xi, L. C. Wang, D. L. Jin, S. Y. Guo and Y. F. Yuan, *Electrochim. Acta*, 2012, **78**, 392–397.
12 B. Lu, X. Li, T. Wang, E. Xie and Z. Xu, *J. Mater. Chem. A*, 2013, **1**, 3900–3906.
13 C. L. Li, J. Yuan, B. Y. Han and W. F. Shangguan, *Int. J. Hydrogen Energy*, 2011, **36**, 4271–4279.
14 Y. Liu, L. Yu, Y. Hu, C. F. Guo, F. M. Zhang and X. W. Lou, *Nanoscale*, 2012, **4**, 183–187.
15 F. S. Cai, Z. H. Yuan, Y. Q. Duan and L. J. Bie, *Thin Solid Films*, 2011, **519**, 5645–5648.
16 C. Gao, X. Li, B. Lu, L. Chen, Y. Wang, F. Teng, J. Wang, Z. Zhang, X. Pan and E. Xie, *Nanoscale*, 2012, **4**, 3475–3481.
17 H.-J. Wang and S.-C. Lee, *Mater. Trans.*, 2009, **50**, 2329–2334.
18 S. Y. Chang, S. F. Chen and Y. C. Huang, *J. Phys. Chem. C*, 2011, **115**, 1600–1607.
19 Q. Gu, J. L. Long, Y. G. Zhou, R. S. Yuan, H. X. Lin and X. X. Wang, *J. Catal.*, 2012, **289**, 88–99.
20 S. N. Chai, G. H. Zhao, P. Q. Li, Y. Z. Lei, Y. N. Zhang and D. M. Li, *J. Phys. Chem. C*, 2011, **115**, 18261–18269.

21 S. Shah, M. C. Benson, L. M. Bishop, A. M. Huhn, R. E. Ruther, J. C. Yeager, Y. Z. Tan, K. M. Louis and R. J. Hamers, *J. Mater. Chem.*, 2012, **22**, 11561–11567.
22 S. Ponja, S. Sathasivam, N. Chadwick, A. Kafizas, S. M. Bawaked, A. Y. Obaid, S. Al-Thabaiti, S. N. Basahel, I. P. Parkin and C. J. Carmalt, *J. Mater. Chem. A*, 2013, **1**, 6271–6278.
23 L. Xu, E. M. P. Steinmiller and S. E. Skrabalak, *J. Phys. Chem. C*, 2012, **116**, 871–877.
24 C. T. Gao, X. D. Li, B. G. Lu, L. L. Chen, Y. Q. Wang, F. Teng and J. T. Wang, *Nanoscale*, 2012, **4**, 3475–3481.
25 R. Zhang, H. Wu, D. D. Lin and W. Pan, *J. Am. Ceram. Soc.*, 2009, **92**, 2463–2466.
26 M. Hirano, H. Dozono and T. Kono, *Mater. Res. Bull.*, 2011, **46**, 1384–1390.
27 E. M. El-Maghraby, *Phys. B*, 2010, **405**, 2385–2389.
28 A. M. Nie, J. B. Liu, Q. Q. Li, Y. C. Cheng, C. Z. Dong, W. Zhou, P. Wang, Q. X. Wang, Y. Yang, Y. H. Zhu, Y. W. Zeng and H. T. Wang, *J. Mater. Chem.*, 2012, **22**, 10665–10671.
29 Z. Y. Zhang, C. L. Shao, X. H. Li, Y. Y. Sun, M. Y. Zhang, J. B. Mu, P. Zhang, Z. C. Guo and Y. C. Liu, *Nanoscale*, 2013, **5**, 606–618.
30 L. Zhang, G. Q. Zhang, H. B. Wu, L. Yu and X. W. Lou, *Adv. Mater.*, 2013, **25**, 2589–2593.
31 G. Q. Zhang, L. Yu, H. E. Hoster and X. W. Lou, *Nanoscale*, 2013, **5**, 877–881.
32 W. Ni, F. X. Liang, J. G. Liu, X. Z. Qu, C. L. Zhang, J. L. Li, Q. Wang and Z. Z. Yang, *Chem. Commun.*, 2011, **47**, 4727–4729.
33 X. Xu, J. Liang, H. Zhou, D. M. Lv, F. X. Liang, Z. L. Yang, S. J. Ding and D. M. Yu, *J. Mater. Chem. A*, 2013, **1**, 2995–2998.
34 Z. W. Niu, Z. Z. Yang, Z. B. Hu, Y. F. Lu and C. C. Han, *Adv. Funct. Mater.*, **13**, 949–954.
35 M. Yang, J. Ma, Z. W. Niu, X. Dong, H. F. Xu, Z. K. Meng, Z. G. Jin, Y. F. Lu, Z. B. Hu and Z. Z. Yang, *Adv. Funct. Mater.*, 2005, **15**, 1523–1528.
36 Z. Z. Yang, Z. W. Niu, Y. F. Lu, Z. B. Hu and C. C. Han, *Angew. Chem., Int. Ed.*, 2003, **42**, 1943–1945.
37 M. Yang, J. Ma, Z. Z. Yang and Y. F. Lu, *Angew. Chem., Int. Ed.*, 2005, **44**, 6727–6730.
38 P. Si, S. J. Ding, J. Yuan, X. W. Lou and D. H. Kim, *ACS Nano*, 2011, **5**, 7617–7626.
39 S. J. Ding, J. S. Chen and X. W. Lou, *Adv. Funct. Mater.*, 2011, **21**, 4120–4125.
40 E. J. Wang, T. He, L. S. Zhao, Y. M. Chen and Y. A. Cao, *J. Mater. Chem.*, 2011, **21**, 144–150.
41 Z. Y. Liu, D. D. Sun, P. Guo and J. O. Leckie, *Nano Lett.*, 2007, **7**, 1081–1085.
42 G. R. Yang, Q. Zhang, W. Chang and W. Yan, *J. Alloys Compd.*, 2013, **580**, 29–36.
43 Y. Wen, B. T. Liu, W. Zeng and Y. H. Wang, *Nanoscale*, 2013, **5**, 9739–9746.
44 D. F Hou, X. L. Hu, P. Hu, W. Zhang, M. F. Zhang and Y. H. Huang, *Nanoscale*, 2013, **5**, 9764–9772.
45 Y. Xu and M. A. A. Schoonen, *Am. Mineral.*, 2000, **85**, 543–556.
46 J. Nayak, S. N. Sahu, J. Kasuya and S. Nozaki, *Appl. Surf. Sci.*, 2008, **254**, 7215–7218.
47 M. Zhou, J. Bao, M. S. Tao, R. Zhu, Y. Q. Zeng, Z. W. Wei and Y. Xie, *Chem. Commun.*, 2012, **48**, 3439–3441.
48 C. Q. Zhu, B. G. Lu, Q. Su, E. Q. Xie and W. Lan, *Nanoscale*, 2012, **4**, 3060–3064.
49 B. G. Lu, C. Q. Zhu, Z. X. Zhang, W. Lan and E. Q. Xie, *J. Mater. Chem.*, 2012, **22**, 1375–1379.
50 P. S. Archana, R. Jose, C. Vijila and S. Ramakrishna, *J. Phys. Chem. C*, 2009, **113**, 21538–21542.
51 S. S. Lee, H. W. Bai, Z. Y. Liu and D. D. Sun, *Int. J. Hydrogen Energy*, 2012, **37**, 10575–10584.

